Electronic Supplementary Material (ESI) for Energy & Environmental Science.

Electronic Supplementary Information

Deconvolution of Intermixed Redox Processes in Ni-based Cation-Disordered Li-Excess Cathodes

Tzu-Yang Huang[1, 2], Matthew J. Crafton[1, 2], Yuan Yue[2], Wei Tong[2], and Bryan D. McCloskey[1, 2, ⋆]

[1]*Department of Chemical and Biomolecular Engineering, University of California–Berkeley, Berkeley, California 94720, United States*

[2]*Energy Storage and Distributed Resources Division, Lawrence Berkeley National Laboratory, Berkeley, California 94720, United States*

⋆Correspondence: bmcclosk@berkeley.edu

Note S1. Isotopic Enrichment

A known amount of $Li_{1.15}Ni_{0.45}Ti_{0.3}Mo_{0.1}O_{1.85}F_{0.15}$ (NTMF) powder was weighed (243.2 mg) on a 2 mL combustion boat (VWR) and placed in a Lindberg Blue Mini Mite Tube Furnace (Thermo Scientific). The tube (Alumina, 20" length, 1" OD, Coorstek) was sealed using Swagelok Ultra-Torr fittings that allow connection to 20 cm stainless-steel capillaries (1/16" OD, VICI). The capillaries allow the tube to be connected to various attachments: 1) an expandable membrane (airtight heat-sealable aluminum pouch) that allows heated gas volume expansion; 2) a closed $^{18}O_2$ gas tank (97 at%, Sigma Aldrich) that controls the dosage of $^{18}O_2$. In addition, a cleaned, N_2-purged, and emptied 1 mL gas sample loop (1/16" OD stainless-steel capillary, VICI) under static vacuum was attached to the furnace through a closed valve, which could be toggled on and off to extract headspace gas at the end of the enrichment process. The tube furnace with all fittings was leak-tested and purged with N_2 for ≥ 3 hours. A known volume (15 mL, 1 atm, room temperature) of $^{18}O_2$ was introduced into the furnace while the closed system was allowed to equilibrate at the recorded ambient temperature and pressure (1 atm). The enclosed samples were heated to 600 °C for 6 hours to induce isotopic exchange. After cooling and headspace gas sampling, the ^{18}O-enriched powder was transferred to an Ar-filled glove box with minimized exposure to the ambient (< 5 min) to avoid substantial change in surface native carbonate (NACN) content. To acquire isotopic enrichment level in the NTMF lattice, an oxygen balance on ^{18}O was performed by comparing the closed system before (denoted by prime symbol, natural abundance of ^{18}O is 0.2%) and after isotopic exchange, where n_i and ρ_i represents the molar amount and ^{18}O isotopic fraction of species i, respectively:

$$\begin{aligned} &2 \times n'_{O_2} \times 97\% + 1.85 \times n'_{NTMF} \times 0.2\% + 3 \times n'_{NACN} \times 0.2\% \\ &\quad = 2 \times n_{O_2} \times \rho_{O_2} + 2 \times n_{CO_2} \times \rho_{CO_2} + 1.85 \times n_{NTMF} \times \rho_{NTMF} + 3 \times n_{NACN} \times \rho_{NACN} \end{aligned} \tag{S.1}$$

With the assumption that the net amount of headspace O_2 remains constant before and after isotopic exchange ($n'_{O_2} = n_{O_2}$), mass-spectrometry analysis on the sampled headspace gas allows quantification of ρ_{O_2}, ρ_{CO_2} , and n_{CO_2}/n_{O_2}. The ^{18}O-enriched powder was titrated by 10 M H_2SO_4 to measure n_{NACN} and ρ_{NACN}, as shown in Table S1. Notice that $n'_{NACN} \approx n_{CO_2} + n_{NACN}$ and $\rho_{CO_2} \approx \rho_{NACN}$, which suggests that solid NACN and headspace CO_2 almost reach equilibrium between thermal decomposition and re-deposition during the isotopic exchange process. On the whole, substituting all measurable variables in Equation (S.1) for known quantities determines ρ_{NTMF}, namely the bulk mean ^{18}O enrichment in NTMF lattice.

Table S1. Isotopic Distribution of Native Carbonate (NACN)

Titration [a]: $C^*O_3^{2-} + H^+ \longrightarrow C^*O_2 \uparrow + H_2{}^*O$

Carbonate [b]	Distribution (%)			Enrichment
(μmol g^{-1})	$C^{16,16}O_2$	$C^{16,18}O_2$	$C^{18,18}O_2$	^{18}O (%)
34.6	37.8	44.6	17.6	39.9

[a] Star symbols denote partial ^{18}O enrichment;
[b] Amount normalized to the net weight of NTMF powder.

Table S2. Isotopic Distribution of *in-situ* CO_2 Outgassing

Cut-off Voltage (V)	CO_2 source	Amount [a] (mmol mol^{-1})	Distribution (%)			Enrichment ^{18}O (%)
			$C^{16,16}O_2$	$C^{16,18}O_2$	$C^{18,18}O_2$	
3.0 [b]	NACN	< 0.1	n/a	n/a	n/a	n/a
	Elyte	< 0.1	n/a	n/a	n/a	n/a
3.9	NACN	< 0.1	n/a	n/a	n/a	n/a
	Elyte	< 0.1	n/a	n/a	n/a	n/a
4.0	NACN	< 0.1	n/a	n/a	n/a	n/a
	Elyte	0.3	100.0	< 0.1	0.0	< 0.1
4.1	NACN	< 0.1	n/a	n/a	n/a	n/a
	Elyte	0.4	90.7	9.3	0.0	4.7
4.4	NACN	0.2	37.8	44.6	17.6	39.9
	Elyte	1.0	77.9	22.1	0.0	11.0
4.5	NACN	0.5	37.8	44.6	17.6	39.9
	Elyte	1.4	71.9	28.1	0.0	14.0
4.6	NACN	0.5	37.8	44.6	17.6	39.9
	Elyte	1.7	84.9	15.1	0.0	7.5
4.7	NACN	0.6	37.8	44.6	17.6	39.9
	Elyte	4.9	86.9	13.1	0.0	6.5
4.8	NACN	1.0	37.8	44.6	17.6	39.9
	Elyte	7.1	86.6	13.4	0.0	6.7

[a] Amount normalized to the net mole of active material, NTMF;
[b] Uncharged cathode is displayed at the average OCV.

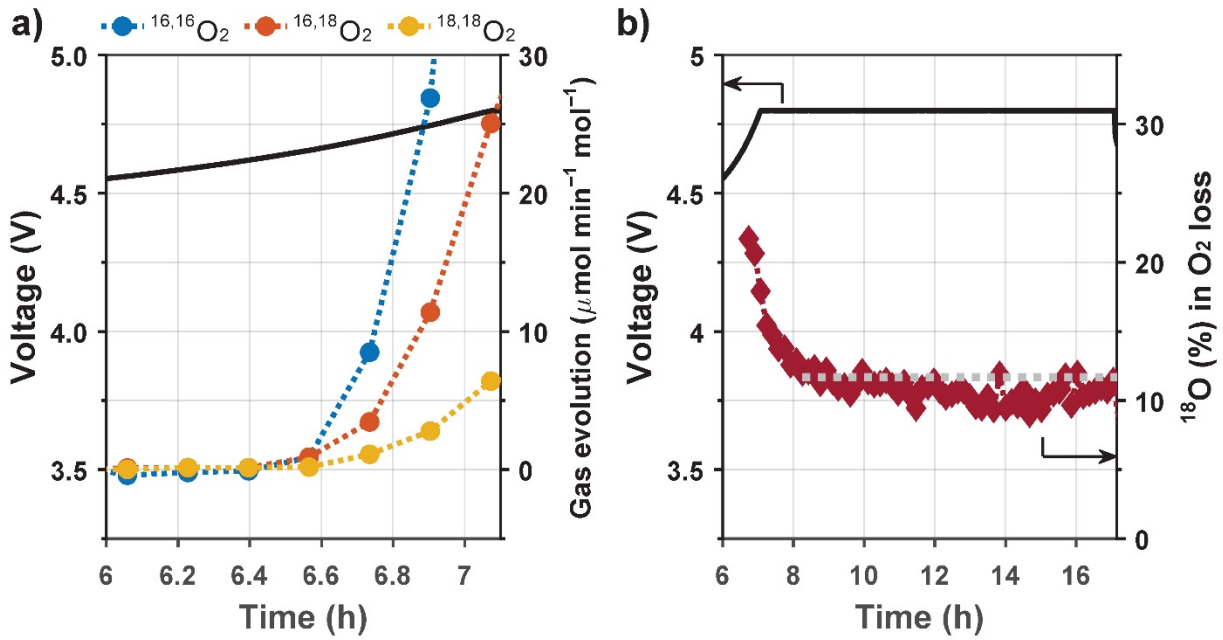

Figure S1. *In-situ* O_2 loss (DEMS) for NTMF charged to 4.8 V (vs. Li/Li^+). (a) Onset of O_2 evolution along the voltage profile (black line), indicating almost identical onset potential and electrochemical origin for the three isotopic O_2 species. (b) ^{18}O enrichment of O_2 (red solid markers) in the sampled headspace gas at each instant after O_2 onset. Gray horizontal dotted line denotes the lattice bulk mean value. Initial higher gaseous ^{18}O enrichment than the solid-state bulk mean value implies that O_2 loss begins from the NTMF crystal surface, where gradient ^{18}O enrichment is expected.

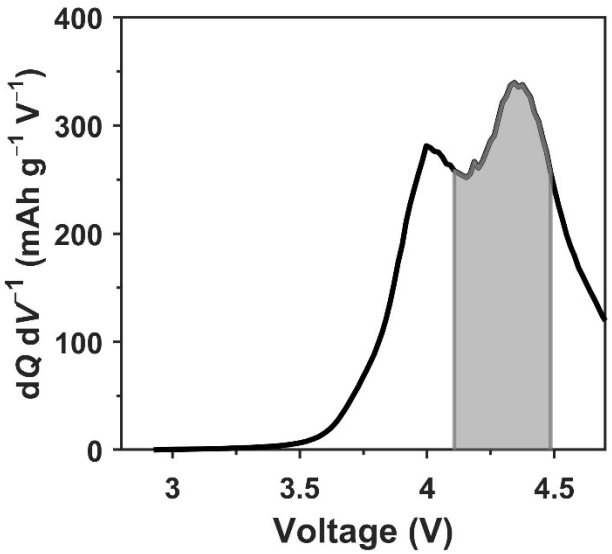

Figure S2. First-charge differential capacity analysis ($dQ\ dV^{-1}$) for NTMF tested at the constant current rate of 0.1 $Li^+\ h^{-1}$ without voltage hold. The enclosed area of the gray-shaded region equals the net electron transfer measured by the potentiostat at the voltage range between 4.1 V and 4.5 V.

Note S2. Disproportionation of Various Lattice Oxidized Oxygen Species

While we display O^- as the lattice oxidized oxygen in Equation (1) and Figure 3, the possible existence of other oxidized oxygen species, such as superoxide (O_2^-), cannot be ruled out. Here we simplify the charge compensation, during the electrochemical operation, fulfilled by lattice oxygen as the following equation, where $0 \leq \omega < 2$ and $2\,(2-\omega)$ electrons in the lattice are ultimately delivered to the external circuit due to lattice-delithiation (remove Li^+ from the lattice) coupled with lattice-electroneutrality:

$$[O^{2-} + O^{2-}]_{\text{lattice}} \longrightarrow [O^{\omega-} + O^{\omega-}]_{\text{lattice}} + 2\,(2-\omega)\,e^- \tag{S.2}$$

In the strong acid environment, namely 10 M H_2SO_4 titration, we posit that the dissolved oxidized oxygen species from NTMF lattice preferentially dimerize due to a close frontier-orbital energy and symmetry match, followed by the disproportionation reaction:

$$[O \cdots\cdots O]^{2\omega-}\,(aq) + 2\omega\,H^+ \longrightarrow \frac{2-\omega}{2}\;O_2 \uparrow + \omega\,H_2O \tag{S.3}$$

With each gaseous O_2 arising from disproportionation reactions, measured by TiMS, we can backcalate O-redox capacity of 4 e^- by adopting the stoichiometric coefficients in both Equation (S.2) and Equation (S.3) ($2\,(2-\omega)/(\frac{2-\omega}{2}) = 4$), which is independent of formal oxidation state of lattice oxidized oxygen species. This analysis suggests that the acid titration technique developed in this work is generalizable to quantify O-redox capacity contributed by a wide variety of lattice oxidized oxygen species.

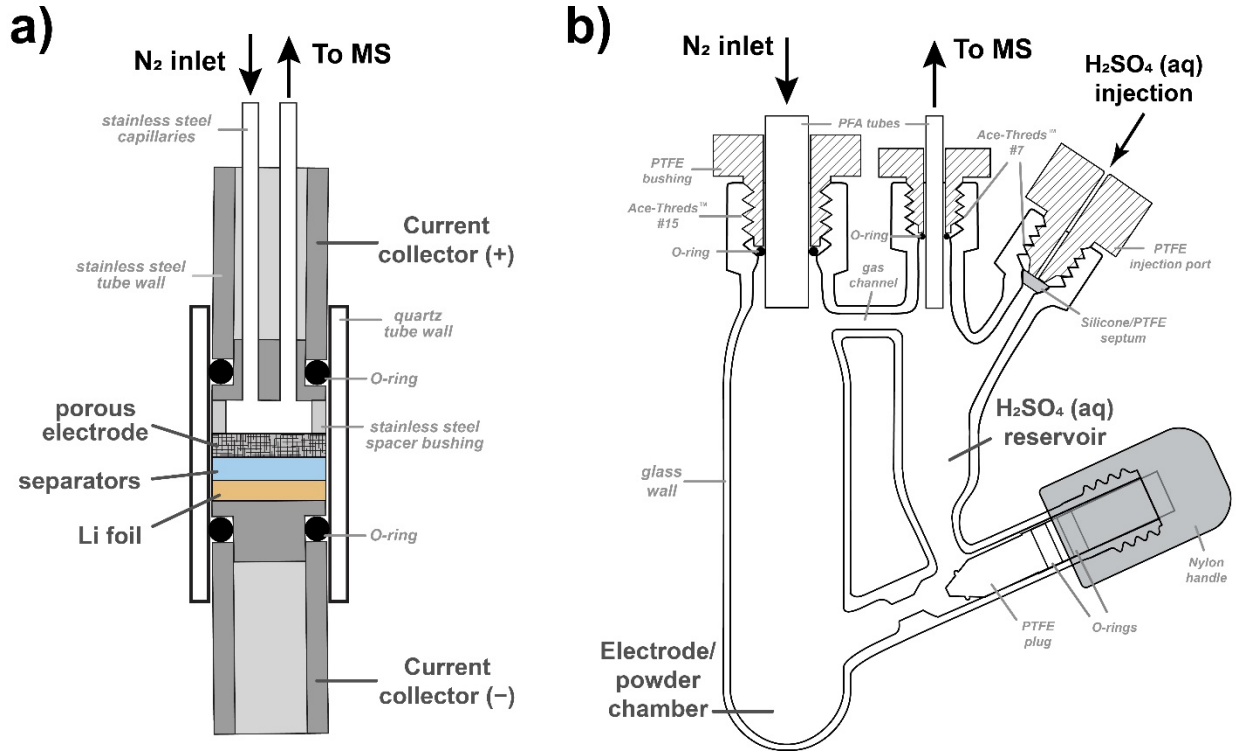

Figure S3. Cell configuration schematics. (a) Electrochemical cell[1,2] with the center quartz tubular section wrapped by a Swagelok perfluoroalkoxy (PFA) union fitting. (b) Titration glass cell, on which the upper ends of PFA tubes are fastened by Valco column end fittings that allow connection to either a carrier gas supply system or the mass-spectrometer gas sample transfer line. The entire setup was leak-tested before each electrochemical measurement or titration experiment.

Note S3. Decoupling mixed O_2 release by TiMS

A mixture of ^{18}O tagged and untagged O_2 evolves when an extracted charged cathode is titrated with 10 M H_2SO_4. The molar amount of O_2 released from the disproportionation reaction (Equation (1)) is denoted by m_1 and can be calculated from the following equation, where n_i and ρ_i represents the molar amount and ^{18}O isotopic fraction of species i, respectively:

$$m_1 = \frac{n_{^{16,18}O_2} + 2\, n_{^{18,18}O_2}}{2\, \rho_{\mathrm{NTMF}}} \tag{S.4}$$

Water oxidation (Equation (2)) emitting m_2 of O_2 can be quantified accordingly:

$$m_2 = n_{^{16,16}O_2} - (m_1 - n_{^{16,18}O_2} - n_{^{18,18}O_2}) \tag{S.5}$$

The values of m_1 and m_2 for titrated cathodes at various cut-off voltages are summarized in Table S3 for comparison.

Table S3. Decoupled O_2 Release During Acid Titration

Cut-off Voltages [a](V)	Net O_2 (mmol mol^{-1}) [b]	Distribution (%)			O_2 [c]	O_2 [d]
		$^{16,16}O_2$	$^{16,18}O_2$	$^{18,18}O_2$	m_2	m_1
3.0 [e]	< 0.1	n/a	n/a	n/a	< 0.1	< 0.1
3.9	17.4	98.6	0.7	0.7	15.9	1.5
4.0	36.9	98.7	1.0	0.3	34.3	2.7
4.1	61.8	98.8	1.0	0.2	58.3	3.5
4.5	166.9	94.6	4.4	1.0	121.7	45.2
4.7	183.0	94.5	4.8	0.7	133.9	49.2

[a] Cut-off voltage of each extracted cathode;
[b] Amount normalized to the net mole of active material, NTMF;
[c] Equation (2) and Equation (S.5);
[d] Equation (1) and Equation (S.4);
[e] Uncharged cathode is displayed at the average OCV.

Table S4. Effect of Charge Current on 4.5 V-Cathodes

Charge Rates [a] ($Li^+ h^{-1}$)	Net O_2 (mmol mol^{-1}) [b]	Distribution (%)			O_2 [c]	O_2 [d]
		$^{16,16}O_2$	$^{16,18}O_2$	$^{18,18}O_2$	m_2	m_1
0.05	163.4	95.4	3.6	1.0	122.4	41.0
0.1	166.9	94.6	4.4	1.0	121.7	45.2
0.5	165.4	95.3	3.7	1.0	124.1	41.2

[a] After the constant-rate charge to 4.5 V, cathodes underwent a voltage hold until the current dropped below an equivalent threshold 0.01 $Li^+ h^{-1}$ (2.95 mA g^{-1});
[b] Amount normalized to the net mole of active material, NTMF;
[c] Equation (2) and Equation (S.5);
[d] Equation (1) and Equation (S.4);

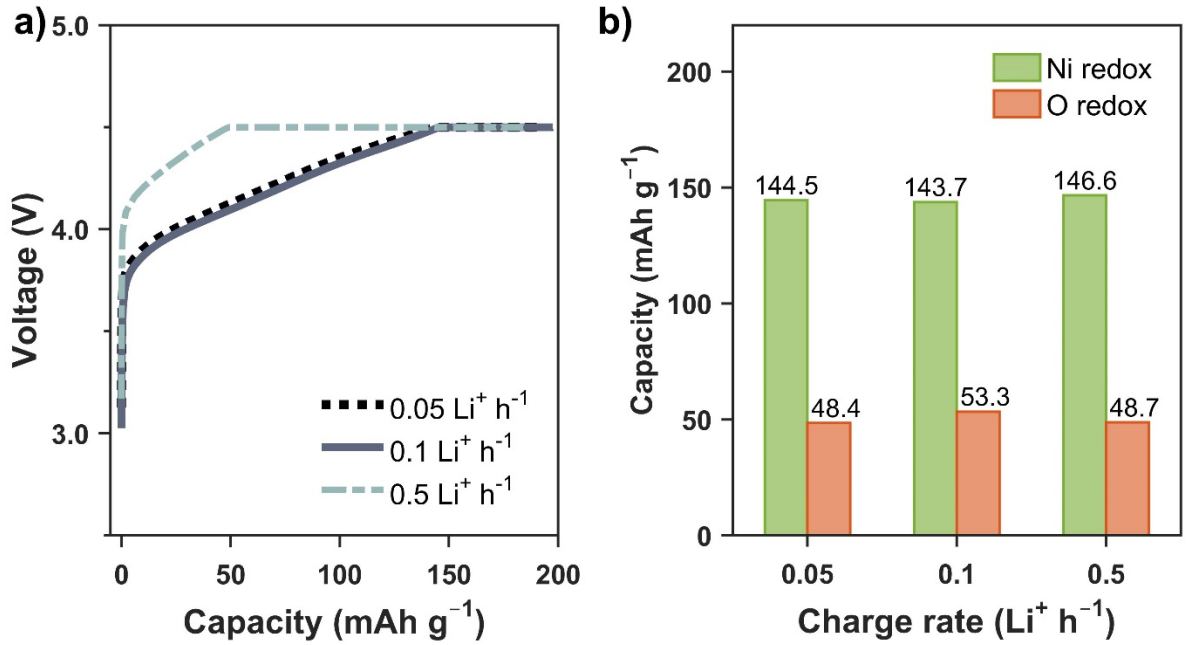

Figure S4. Effect of charge current on the relative contribution of redox processes. (a) Voltage profiles of ^{18}O-enriched NTMF electrodes during constant-rate charges, ranging from 0.05 $Li^+ h^{-1}$ (14.8 mA g^{-1}) to 0.5 $Li^+ h^{-1}$ (148 mA g^{-1}), followed by a voltage hold at 4.5 V vs. Li/Li^+ until the current dropped below the same threshold 0.01 $Li^+ h^{-1}$ (2.95 mA g^{-1}). (b) Deconvoluted capacities of Ni redox (green bar) and oxygen redox (orange bar) quantified by TiMS, suggesting almost identical relative contribution of each individual redox processes even though the electrodes experience various amount of time at a cut-off voltage of 4.5 V.

Note S4. Pourbaix Diagrams

To understand the instability of NTMF immersed in acidic aqueous solutions, we analyze the solid-aqueous equilibria[3] of selected model metal-oxide materials that have transition-metal ions (TM) with: 1) similar oxidation states as TM in delithiated NTMF; 2) octahedral coordination in rocksalt-like lattices. All Pourbaix diagrams were generated through open-source Python Materials Genomics (pymatgen)[4] packages, which adopt a formalism[5] combining *ab initio* calculated solid-state energies (acquired by accessing the Materials Project[6] database) with experimentally tabulated aqueous-state free energies to predict solid-aqueous equilibria. Notice that the Materials Project database is actively updated so the converged energy values and the Pourbaix diagrams presented in this work may be subject to slight variation.

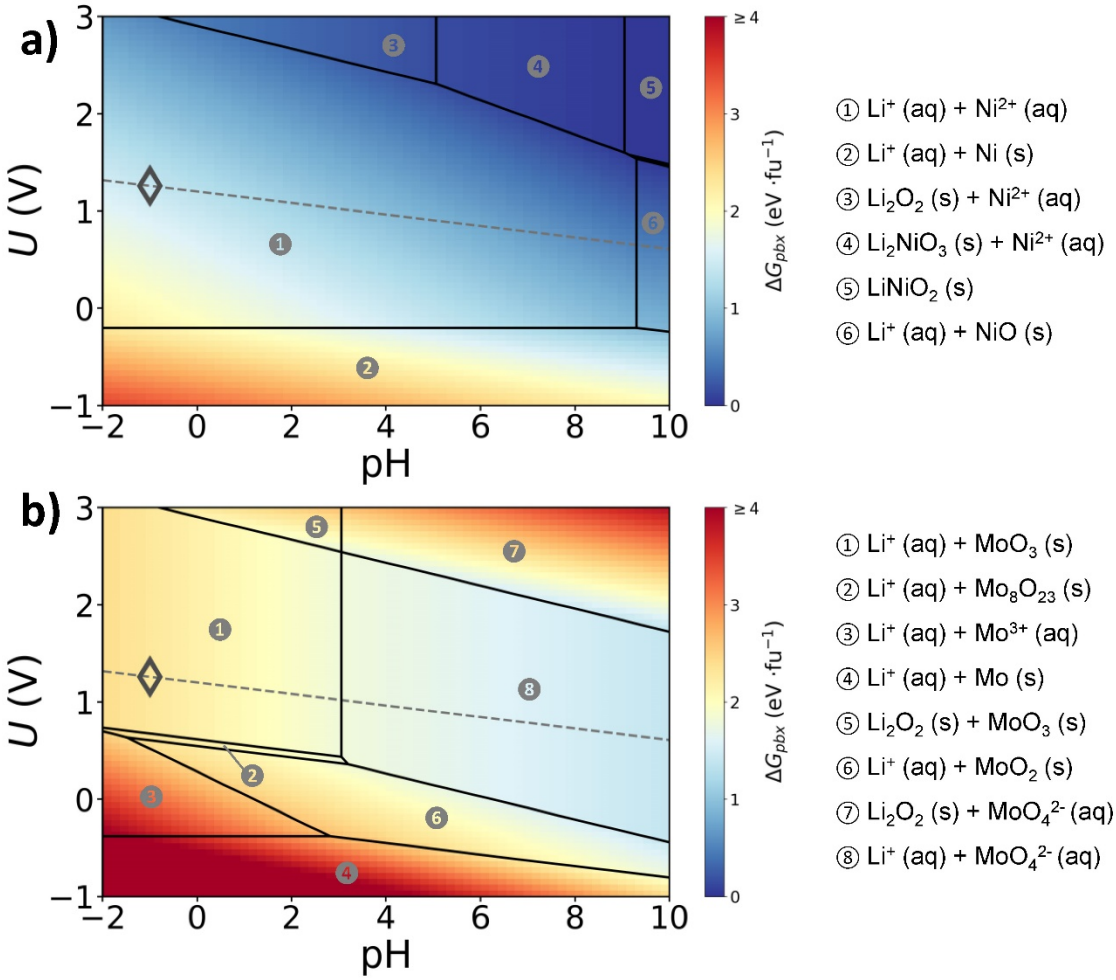

Figure S5. Stability of Ni^{3+} and Mo^{6+} in aqueous environment. Pourbaix Diagrams of (a) $LiNiO_2$ (Material ID: mp-25411) and (b) Li_4MoO_5 (Material ID: mp-19117). Solid-aqueous equilibria and instability maps are calculated and plotted through Python Materials Genomics (pymatgen) packages.[4–7] Each aqueous ion concentration is 10^{-6} M. Instability of the initial solid material is measured by ΔG_{pbx},[7] normalized to the formula unit ($LiNiO_2$ and Li_4MoO_5, respectively). Gray dashed lines denote the O_2/H_2O equilibrium potential with trace O_2 approximated as 0.01 bar. Hollow gray diamonds indicate the pH and external potential (vs. SHE) exerted near the $LiNiO_2$ or Li_4MoO_5 solid surface during the acid titration (10 M H_2SO_4 with trace O_2).

Figure S5 presents Pourbaix diagrams of $LiNiO_2$ and Li_4MoO_5 (Material IDs: mp-25411and mp-19117, respectively),[6] which are examined first to measure the instability of Ni^{3+} and Mo^{6+} in aqueous solutions. In a conventional Pourbaix diagram, each non-vertical line represents an electron-transfer-involving equilibrium potential (vs. SHE) between two groups of species neighboring the line, while each enclosed domain suggests thermodynamically the most stable states at given pH values and voltages applied externally. For example, solid $LiNiO_2$ is prone to form Li^+ (aq) and Ni^{2+} (aq) when immersed in our acid titrant: 10 M H_2SO_4 with trace O_2 (approximated as 0.01 bar), which corresponds to pH ≈ -1 and $U \approx 1.26$ V (vs. SHE) of O_2/H_2O equilibrium potential exerted near the $LiNiO_2$ surface, as labelled by the dark grey hollow diamond in Figure S5a. The driving force for thermodynamically metastable $LiNiO_2$ to decompose into corresponding stable species can be measured by a relative free energy, ΔG_{pbx} [7] as a function of pH and applied U, introduced recently in the corrosion community to complement the conventional Pourbaix diagram. The colormap in Figure S5a displays the quantities of ΔG_{pbx}(pH, U) that are defined as the free energy (taking H^+, H_2O, and electrons into account) of the initial metastable material

(i.e., $LiNiO_2$) minus its decomposition products' free energy. Accordingly, the free energy change of the following reaction is $-\Delta G_{pbx}$ by definition ($\Delta G_{(S.6)} = -\Delta G_{pbx}$):

$$LiNiO_2 + 4\,H^+ + e^- \longrightarrow Li^+\,(aq) + Ni^{2+}\,(aq) + 2\,H_2O \quad (S.6)$$

A redox couple, most probably O_2/H_2O in the acid titration environment, must exist to provide the electron for Equation (S.6). Here we posit that trace O_2 reaches thermodynamic equilibrium (quasi-equilibrium) with H_2O ($\Delta G_{(S.7)} \simeq 0$):

$$2\,H_2O \longrightarrow O_2 + 4\,H^+\,(aq) + 4\,e^- \quad (S.7)$$

The net decomposition reaction, which must satisfy electroneutrality, combines Equation (S.6) with Equation (S.7) and the net thermodynamic driving force can be therefore determined ($\Delta G_{(S.8)} = -4\,\Delta G_{pbx} + \Delta G_{(S.7)}$):

$$4\,LiNiO_2 + 12\,H^+ \longrightarrow 4\,Li^+\,(aq) + 4\,Ni^{2+}\,(aq) + O_2 \uparrow + 6\,H_2O \quad (S.8)$$

As the decomposition of $LiNiO_2$ (Equation (S.8)) during the acid titration involves electron transfer, the driving force can also be interpreted as potential U_j through the following correlation, where ν_j is the number of electrons transferred in reaction *j* and *F* is Faraday's constant:

$$\Delta G_j = -\nu_j F U_j \quad (S.9)$$

As a multi-electron-transfer reaction is usually kinetically sluggish, a decomposition reaction (e.g., Equation (S.8)) requires adequate potential difference to proceed forward. With known ΔG_{pbx} in Figure S5a and $\nu_{(S.8)}$ for Equation (S.8), the driving force of water oxidation by $LiNiO_2$ (Ni^{3+}) can be measured by $U_{(S.8)}$ = 1.38 V, which is considered large enough to drive the reaction because we have experimentally observed O_2 release when titrating pristine $LiNiO_2$ powder.

On the other hand, Li^+ (aq) and MoO_3 are the predicted products when Li_4MoO_5 is titrated by 10 M H_2SO_4 (Figure S5b), which suggests that the decomposition of Mo^{6+}-containing oxide does not favor electron transfer and therefore does not warrant water oxidation (no necessity for Equation (S.7) to supply electrons). Despite limited solubility of solid MoO_3, we expect Mo^{6+}-containing species from NTMF decomposition in strong acid is totally dissolved, as we observed that the final solution after titrating pristine NTMF powder is entirely transparent without any precipitate. MoO_3 has also been shown to be more soluble as the acid concentration increases[8] and its molar solubility (~ 0.04 M) is reasonably higher than the Mo concentration (~ 0.003 M) at the end of titration. As a result, analysis on solid-aqueous equilibria of the first two model metal-oxide materials predicts that during the acid titration, Ni^{3+} is prone to oxidize water and induce O_2 release while Mo^{6+} is likely to dissolve without electron transfer, which agrees well with TiMS results (Table S3).

Even though high-valent Ni exists in both delithiated NTMF (DRX in this work) and delithiated Ni-Mn-Co layered oxides (NMC in our previous works[9–11]), no detectable water- oxidation O_2 releases when titrating charged NMC electrodes. To compare their thermodynamic instability during the acid titration, we analyze the solid-aqueous equilibria of two model TM-oxides deriving from $LiNiO_2$ (with 25% of Ni replaced by Ti^{4+} or Mn^{4+}): 1) $LiNi_{0.75}Ti_{0.25}O_2$ (Battery ID: mp-763760_Li; Material ID: mp-756601); 2) $LiNi_{0.75}Mn_{0.25}O_2$ (Battery ID: mp-1177345_Li; Material ID: mp-1177345).[6,12] These two model oxides are selected in approximate analogy to different local lattice environments of Ni^{3+} in NTMF and NMC. Figure S6 shows Pourbaix diagrams and ΔG_{pbx} maps of $LiNi_{0.75}Ti_{0.25}O_2$ and $LiNi_{0.75}Mn_{0.25}O_2$, respectively. Through the same analysis procedures applied on $LiNiO_2$, the net thermodynamic driving force of decomposing oxides in conjunction with oxidizing water can be determined:

$$\mathrm{LiNi_{0.75}Ti_{0.25}O_2} + \frac{5}{2}\,\mathrm{H^+} \longrightarrow \mathrm{Li^+\,(aq)} + \frac{3}{4}\,\mathrm{Ni^{2+}\,(aq)} + \frac{1}{4}\,\mathrm{TiO_2} + \frac{1}{8}\,\mathrm{O_2}\uparrow + \frac{5}{4}\,\mathrm{H_2O} \quad \text{(S.10)}$$

$$\mathrm{LiNi_{0.75}Mn_{0.25}O_2} + 3\,\mathrm{H^+} \longrightarrow \mathrm{Li^+\,(aq)} + \frac{3}{4}\,\mathrm{Ni^{2+}\,(aq)} + \frac{1}{4}\,\mathrm{Mn^{2+}} + \frac{1}{4}\,\mathrm{O_2}\uparrow + \frac{3}{2}\,\mathrm{H_2O} \quad \text{(S.11)}$$

As the Equation S.11 involves more electrons transferred than Equation (S.10) ($\nu_{(\mathrm{S.11})} > \nu_{(\mathrm{S.10})}$), the resulting decomposition driving force of Equation (S.11) in potential ($U_{(\mathrm{S.11})}$ = 1.17 V) is significantly smaller than U of Equation (S.10) ($U_{(\mathrm{S.10})}$ = 2.36 V). The difference may explain why water-oxidation O_2 release does not take place at an observable rate for Ni^{3+}-Mn^{4+}-O materials (e.g., delithiated NMC), while Ni^{3+}-Ti^{4+}-O materials (e.g., delithiated NTMF) can efficiently oxidize water. The decomposition product TiO_2 from NTMF is believed to form soluble titanyl sulfate ($TiOSO_4$ (aq))[13,14] in the concentrated H_2SO_4, because the final solution after titrating pristine NTMF powder is entirely transparent without any precipitate. The small decomposition driving force coupled with low solubility of Mn^{4+}-oxides may also be the cause of low leaching efficiency of each TM species (any of Ni, Mn, or Co) from NMC lattice into sulfuric acid solution (< 40% of each TM is dissolved after several days).[15]

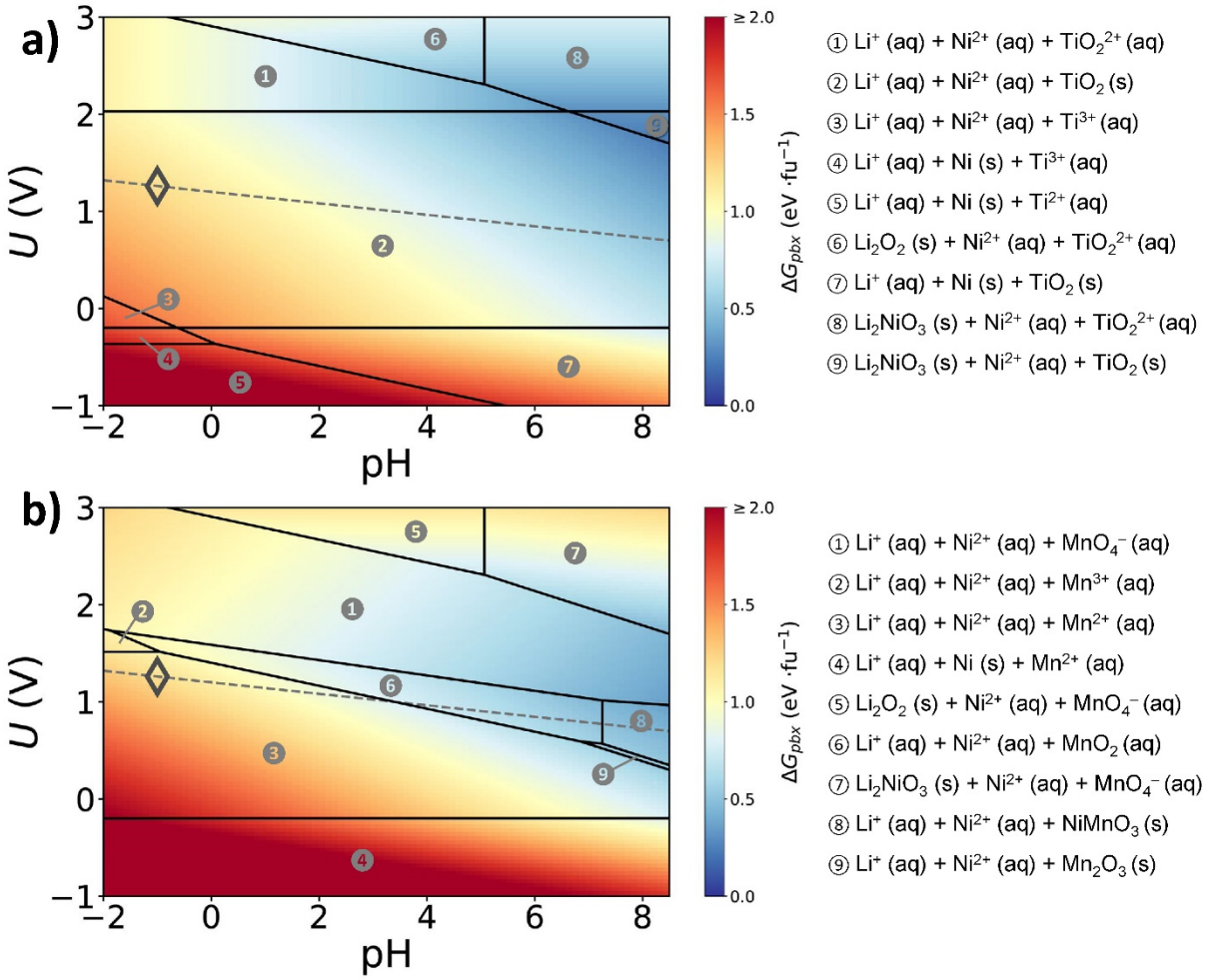

Figure S6. Water-oxidation driving force for Li-Ni$^{2+/3+}$-O materials with different lattice transition-metal chemistries. Pourbaix Diagrams of (a) $LiNi_{0.75}Ti_{0.25}O_2$ (Material ID: mp-756601) and (b) $LiNi_{0.75}Mn_{0.25}O_2$ (Material ID: mp-1177345). Solid-aqueous equilibria and instability maps are calculated and plotted through Python Materials Genomics (pymatgen) packages.[4–7] Each aqueous ion concentration is 10^{-6} M. Instability of the initial solid material is measured by ΔG_{pbx},[7] normalized to the formula unit ($LiNi_{0.75}Ti_{0.25}O_2$ and $LiNi_{0.75}Mn_{0.25}O_2$, respectively). Gray dashed lines denote the O_2/H_2O equilibrium potential with trace O_2 approximated as 0.01 bar. Hollow gray diamonds indicate the pH and external potential (vs. SHE) exerted near the $LiNi_{0.75}Ti_{0.25}O_2$ or $LiNi_{0.75}Mn_{0.25}O_2$ solid surface during the acid titration (10 M H_2SO_4 with trace O_2).

References

1 B. D. McCloskey, D. S. Bethune, R. M. Shelby, G. Girishkumar and A. C. Luntz, *The Journal of Physical Chemistry Letters*, 2011, **2**, 1161–1166.

2 B. D. McCloskey, R. Scheffler, A. Speidel, G. Girishkumar and A. C. Luntz, *Journal of Physical Chemistry C*, 2012, **116**, 23897–23905.

3 M. Pourbaix, *Atlas of electrochemical equilibria in aqueous solutions.*, National Association of Corrosion Engineers, 2d English.

4 S. P. Ong, W. D. Richards, A. Jain, G. Hautier, M. Kocher, S. Cholia, D. Gunter, V. L. Chevrier, K. A. Persson and G. Ceder, *Computational Materials Science*, 2013, **68**, 314–319.

5 K. A. Persson, B. Waldwick, P. Lazic and G. Ceder, *Physical Review B - Condensed Matter and Materials Physics*, 2012, **85**, 235438.

6 A. Jain, S. P. Ong, G. Hautier, W. Chen, W. D. Richards, S. Dacek, S. Cholia, D. Gunter, D. Skinner, G. Ceder and K. A. Persson, *APL Materials*, 2013, **1**, 011002.

7 A. K. Singh, L. Zhou, A. Shinde, S. K. Suram, J. H. Montoya, D. Winston, J. M. Gregoire and K. A. Persson, *Chemistry of Materials*, 2017, **29**, 10159–10167.

8 L. M. Ferris, *Journal of Chemical & Engineering Data*, 1961, **6**, 600–603.

9 S. E. Renfrew and B. D. McCloskey, *ACS Applied Energy Materials*, 2019, **2**, 3762–3772.

10 S. E. Renfrew and B. D. McCloskey, *Journal of The Electrochemical Society*, 2019, **166**, A2762–A2768.

11 S. Ramakrishnan, B. Park, J. Wu, W. Yang and B. D. McCloskey, *Journal of the American Chemical Society*, 2020, **142**, 8522–8531.

12 F. Zhou, M. Cococcioni, C. A. Marianetti, D. Morgan and G. Ceder, *Physical Review B - Condensed Matter and Materials Physics*, 2004, **70**, 1–8.

13 H. Sibum, V. Güther, O. Roidl, F. Habashi, H. Uwe Wolf and C. Siemers, *Ullmann's Encyclopedia of Industrial Chemistry*, 2017, 1–35.

14 I. Szilágyi, E. Königsberger and P. M. May, *Inorganic Chemistry*, 2009, **48**, 2200–2204.

15 E. Billy, M. Joulié, R. Laucournet, A. Boulineau, E. de Vito and D. Meyer, *ACS Applied Materials and Interfaces*, 2018, **10**, 16424–16435.